

Dynamic label-free imaging of lipid nanodomains, Supplementary Material.

G. de Wit^{1§}, J. S. H. Danial^{1§}, P. Kukura^{1*}, M.I. Wallace^{1*}.

Materials and Methods:

Materials. DPhPC, DOPC, POPC, bSM and Chol were obtained from Avanti Polar Lipids. DiI-C18 was obtained from Invitrogen. Lipids purchased were used without further purification, dissolved in chloroform at 50 mg ml⁻¹ and stored at -20°C until use. All other reagents were obtained from Sigma-Aldrich.

DIB formation. DIBs were prepared following our previously reported protocol (36). Briefly, 400 nl droplets of 90 mM 4-(2-hydroxyethyl)-1-piperazineethanesulfonic acid (HEPES) were incubated for 40 minutes in a solution of the required lipids in hexadecane plus 10% [v/v] silicone oil (AR 20) at a concentration of 8.7 mg ml⁻¹ to form a lipid monolayer at the oil-water interface. This concentration is significantly below the solubility limit for our lipid mixtures (**Fig. S4**). Meanwhile, 140 µl of 0.75 % [w/v] ultra low melt agarose was spin-cast onto a plasma-cleaned coverslip at 4000 rpm for 30 s. The agarose-coated cover slip was sealed with a micro-fabricated poly(methyl methacrylate) (PMMA) device (36). 180 µl of 2.8% [w/v] Low melt agarose was used to seal the gap between the coverslip and device. The device was filled with the aforementioned lipid/oil solution. Incubated droplets were transferred to the device after 20 minutes to form a bilayer upon contact with the agarose substrate. Based on our previous work (37), we estimate a maximum bilayer hydrocarbon content of 9.2%. Finally, the device was heated (46 °C) above the transition temperature of bSM, cooled to room temperature and imaged using iSCAT and/or TIRF microscopy.

Experimental Setup. All optical components were obtained from Thorlabs unless mentioned otherwise.

For **iSCAT**, the output of a 662 nm diode laser (Coherent Obis) was adjusted to 2 mm beam diameter before passing through two acousto-optic deflectors (AOD, Gooch and Housego). The two AOD channels are scanned in a saw-tooth by separate, phase-locked function generators (Rigol DG1022) at 79 and 80 kHz, respectively. Both the absolute and relative frequencies are chosen to induce the smallest detectable fluctuations in the background light intensity on the time scale of the camera exposure time. The beam deflected by the AODs is imaged with telecentric lenses onto the back focal plane of an oil immersion 1.42 NA, 60x objective (Olympus PLAPON) after passing through a polarizing beam splitter (PBS). The 662 nm beam under fills the back aperture of the objective to generate a focal spot of ~ 1 µm. A quarter wave plate before the objective causes the p-polarised incident light to be converted to s polarized light after reflection from the sample. The returning light is reflected by the PBS and imaged onto a CMOS camera (Photonfocus MV-D1024-160-CL-8, 10 µm pixels) at 166x or 250x magnification. Schematic for setup is shown in Fig S1. Data in **Fig. 1C** and **Fig. 1D** was recorded with a 445 nm laser, without the dichroic mirrors and fluorescence channel. Data in **Fig. 2A** and **Fig. 2B** were recorded with a 638 nm laser, the remainder of the setup was the same. Data in **Fig. 2C** was recorded with a 532nm laser, without the dichroic mirrors and fluorescence channel and without AOD scanning.

For **TIRF**, a 473 nm diode laser (Crystal Laser) is translated across the back aperture of the objective to totally internally reflect off the sample. The beam is focused onto the back focal plane with a 400 mm lens, to generate a wide field illumination spot with FWHM ~ 15 µm. The

beam is reflected off a 505 nm long pass dichroic and a 605 nm long pass dichroic mirror, which passes the 662nm beam so that both beams are overlapped entering the objective. Fluorescence in the 505 nm to 605 nm window is separated from both the reflected 662nm beam and 473 nm beams by the two dichroic mirrors, and after passing through a 550 nm long pass filter is imaged onto an emCCD camera (Andor iXon3 860).

Experimental conditions for Fig 1. The appearing nanodomains (**Fig. 1C**) were recorded with 445 nm illumination with power density 0.2 kW cm^{-2} . Images were collected at 50 Hz.

Experimental conditions for Fig 2. The dataset for **A** and **B** was recorded with 662 nm illumination with power density 13 kW/cm^2 . Images were collected at 2 kHz. Frames shown have been frame binned to 100 Hz. The data for **A** and **B** has been appended from 3 movies (each of a different nanodomain), rather than to attempt to follow the domain across a typical travel of several 10s of μm . The dataset shown in **C** was recorded with 532 nm illumination with a power density of 20 kW cm^{-2} . Images were collected at 4 kHz, and binned to 400 Hz. Each nanodomain was tracked by fitting a 2D Gaussian in every frame. The trajectories were divided into 100 frame intervals and the average contrast, average FWHM and diffusion coefficient for each interval was calculated. The diffusion coefficient was calculated by fitting the line of best fit to the MSD vs. Δt , for time intervals up to 20 frames (maximum time interval 50 ms), where $D = \text{slope}/4$. In the final plot shown in **Fig. 2C**, the data has been averaged into 0.1% contrast bins.

Experimental conditions for Fig 3. A, B, C, D and E: All compositions shown were recorded using 662 nm illumination at a power density of 13 kW cm^{-2} . Dynamic events have been frame binned to 50 fps for in the frame sequences shown. **Figure 3D** includes data from 749 nanodomains. Data was recorded at 500 Hz, and divided into 50 frame intervals, or 100 ms. For each interval, the average contrast, FWHM and Diffusion coefficient (best linear fit to MSD vs. time for Δt up to 10 frames or 20 ms, where $D = \text{slope}/4$). The FWHM reported here is calculated from the maximum difference in mean contrast between consecutive concentric circles.

iSCAT Image processing. Image processing is achieved by removing any constant background caused by residual reflections and illumination inhomogeneity. To do so, 1000 images are recorded while manually moving the sample stage and each pixel is then replaced by the temporal median value of the frame sequence to generate an optimal flat field image that is independent of the sample. Following division by the flat field image, sample-specific images with shot noise limited sensitivity are obtained. Finding the correct focal point is critical and is automatically achieved by locking the position of the reflected 473 nm beam by feeding back the positional difference to the sample stage Piezo controllers. The feedback loop operates at 20 Hz, keeping the z position within 5 nm of the target. To generate an image containing all the static iSCAT features we performed a stack averaging over the stack of frames acquired. Domains were fitted to Gaussian Point Spread Functions (PSF) to obtain the center and contrast values.

S₀ nanodomains tracking and analysis: Nanodomains were tracked using the ImageJ Trackmate plugin (38) ($Q > 0.15$, max. link 15 px, max. gap = 15 px 2 frames). Domains were then fit to a Gaussian to determine their FWHM. The FWHM reaches a constant, minimum value for domains $< 2\%$ contrast. We assume that the FWHM of the PSF is equal to this value (338.6 nm). Domain radii were determined by deconvolution of this PSF.

L₀ nanodomains tracking and analysis: Nanodomain lifetime was determined as the track lengths returned by Trackmate (38). The nanodomains trajectories were divided into 50 frame

sub-trajectories for which the average HWHM, average contrast and diffusion coefficients were calculated. The data from all sub trajectories was binned into 0.2% contrast intervals, in order to display the binned HWHM and diffusion coefficients as a function of the contrast (**Figs. 3E&F**). Error bars are the standard deviation of the data within each contrast bin.

Microdomains tracking and analysis: Domains were delineated by thresholding a highpass filtered (7 pixels) image to the half maximal intensity. Domains in the resulting binary image were tracked by centroiding. The radius was found from the area of the domain, assuming a circular geometry.

Supplementary Movies

Movie S1: L_o lipid nanodomain appearance.

Movie S2: L_o lipid nanodomain – microdomain fusion.

Movie S3: L_o lipid nanodomain coalescence.

Supplementary Figures.

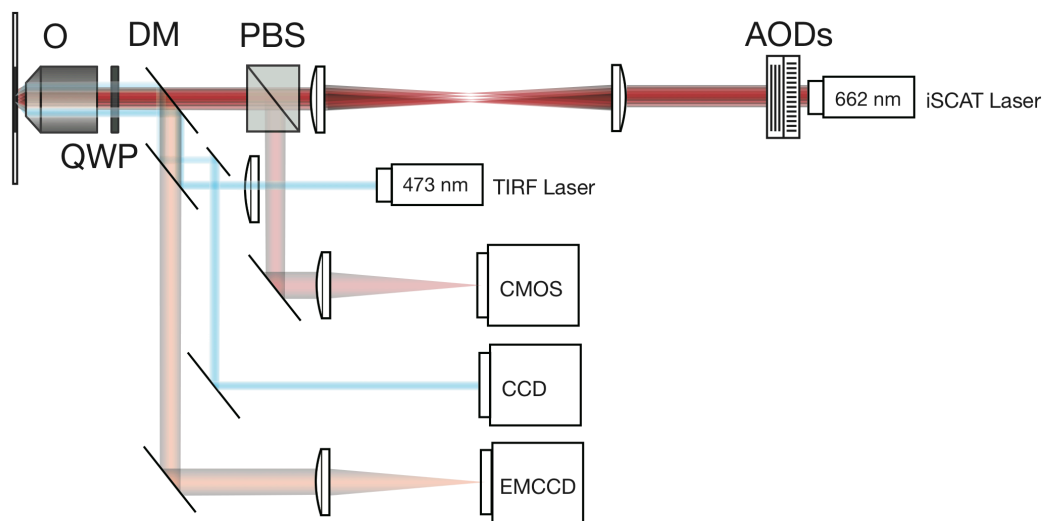


Fig. S1. Diagram of Experimental Setup. AOD, Acousto-Optic Deflector; DM, Dichroic Mirror; O, Objective; PBS, Polarizing Beam Splitter; QWP, Quarter Wave Plate. In essence, iSCAT simply requires the interference between light scattered from the sample and nearby substrate. A high speed CMOS camera then detects this interferometric signal as a perturbation on the large reflected background from the substrate (20).

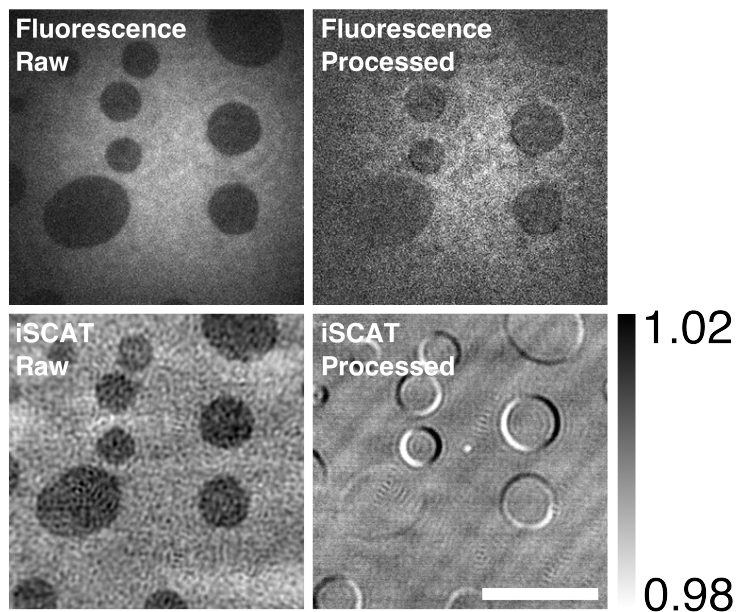


Fig. S2. Comparison of raw and processed TIRF and iSCAT images. Images of domains in a DOPC:bSM (1:1) bilayer with 1 mol% Atto 488. Images were taken at 100 Hz (iSCAT) and 20 Hz (fluorescence). Scale bar 10 μm .

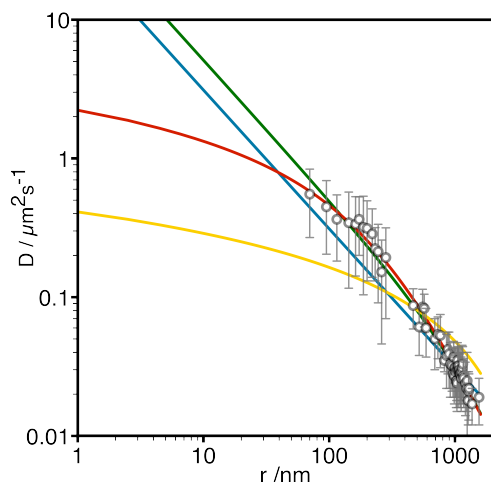


Fig. S3. Tracking of small S_o microdomains. Data was recorded at 500 Hz, using 662 nm illumination at a power density of 0.7 kW cm^{-2} . The radii of domains smaller than the diffraction limit (338.6 nm) were obtained by deconvolution of the PSF. Diffusion coefficient vs. domain radius was fit to the large limit of the Saffman Delbrück (yellow), Guigas-Weiss (green), Petrov-Schwille (blue) and Evans-Sackmann models (red). The Guigas-Weiss model best describes the data (GW: $\chi^2 = 2.957$, $\eta_c = 0.00505 \text{ N s m}^{-2}$, $c = 1.377 \times 10^{-6}$; ES: $\chi^2 = 3.002$, $\eta_m = 0.20596 \text{ N s m}^{-1}$, $b_s = 13561.8 \text{ N s m}^{-3}$; PS: $\chi^2 = 6.110$, $\eta_c = 0.0083 \text{ N s m}^{-2}$, $\eta_m = 2.5 \times 10^{-12} \text{ N s m}^{-1}$; SD: $\chi^2 = 9.02$, $\eta_c = 0.00306 \text{ N s m}^{-2}$, $\eta_m = 1.51 \text{ N s m}^{-1}$). This scaling enables the estimation of S_o and L_o nanodomain radii.

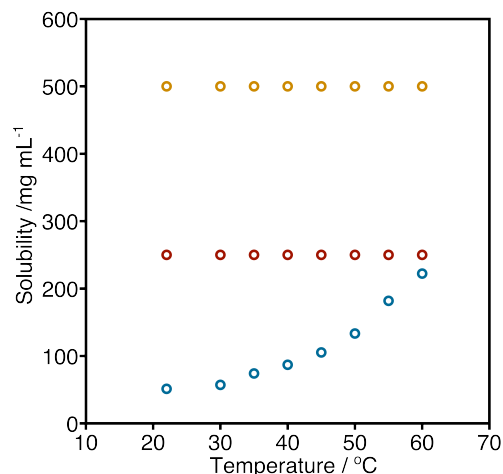


Fig. S4. Solubility of DOPC:bSM 1:1 (blue), DOPC:bSM:Chol 1:1:1 (red) and DOPC:POPC:bSM:Chol 1:1:1:1 (orange) in hexadecane. The solubility of all lipid mixtures is larger the concentration of lipid in oil used in this work (8.7 mg mL^{-1}). With the exception of the solubility of the binary mixture of DOPC:bSM, which increases with temperature, all other compositions do not show a pronounced variation in solubility with temperature.

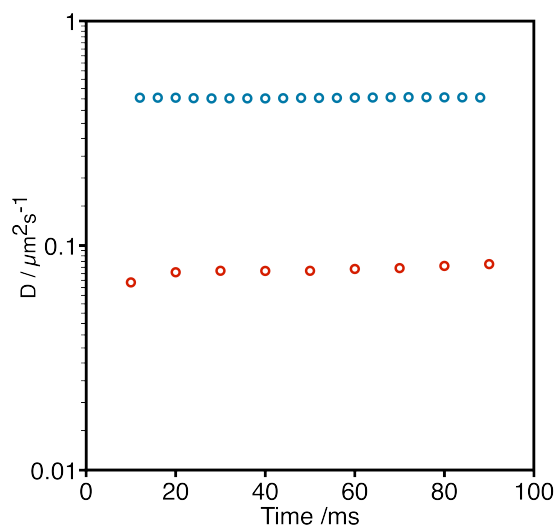


Fig. S5. Tracking of nanodomain (blue) and microdomain (red) diffusion shows invariance with respect to time lag. This suggests domain diffusion is purely Brownian and unrestricted with no anomalous component. These results are in agreement with our previous work where the presence of the hydrated agarose substrate did not affect protein diffusion in DIBs (40).

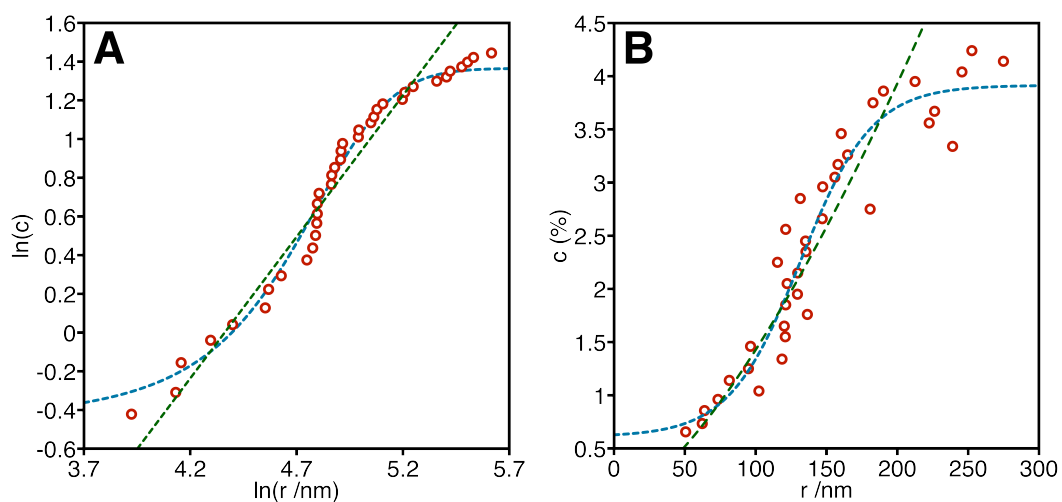


Fig. S6. Logarithmic (A) and linear (B) plots of the variation of the contrast (c) of S_0 domains with radius (r). Dashed lines are power (green, $\ln(c) = 1.462 \ln[r] - 6.377$), and sigmoid (blue, $c = 0.61081 + 3.3037 / \{1 + \exp[(131.72 - r)/25.146]\}$) fits to the data.